High-speed visualization of metal oxide precursor in multiphase AC arc during nanoparticle formation

Tanaka, Manabu
Department of Chemical Engineering, Kyushu University

Saito, Yuki
Department of Chemical Engineering, Kyushu University

Maruyama, Hiroki
Department of Chemical Engineering, Kyushu University

Watanabe, Takayuki
Department of Chemical Engineering, Kyushu University

出版情報：Japanese Journal of Applied Physics. 59 (SH), 2020-04-07. 応用物理学会
バージョン：

High-speed visualization of metal oxide precursor in multiphase AC arc during nanoparticle formation

Manabu Tanaka, Yuki Saito, Hiroki Maruyama, and Takayuki Watanabe*

Department of Chemical Engineering, Kyushu University, Fukuoka, Fukuoka 819-0395, Japan

E-mail: watanabe@chem-eng.kyushu-u.ac.jp

The purpose of the present work is to elucidate the formation mechanism of metal oxide nanoparticles in a multiphase AC arc, which is one of the most attractive thermal plasma sources. Lanthanum oxide nanoparticles was focused on the basis of the spectroscopic diagnostics and thermodynamic consideration. The dynamic behavior of lanthanum vapor and lanthanum monoxide in the multiphase AC arc was visualized by a high-speed camera through band-pass filter optics. Furthermore, two-dimensional temperature field of the multiphase AC arc was successfully estimated by the same camera system based on the relative intensity method, which includes the emissions from lanthanum atom and lanthanum ion. Obtained temperature profile and the intensity profile of lanthanum and lanthanum monoxide suggested that the oxidation from lanthanum to lanthanum monoxide occurred following thermodynamic equilibrium. These understanding fundamental phenomena in thermal plasma nanofabrication process enables to expand the capability of thermal plasma for innovative material processing.

1. Introduction

Thermal plasmas have been widely applied to many industrial fields because of their unique advantages: extremely high temperature over than 10,000 K, high enthalpy to enhance reaction kinetics, rapid quenching capability to produce chemical non-equilibrium materials, and controllability of reaction atmosphere in accordance with required chemical reaction such as oxidation or reduction. These advantages extend the capability of thermal plasmas for various applications in industrial field [1-4].

Thermal plasmas are mostly generated through electrical methods based on direct current, alternating current arc discharges, inductively coupled radio-frequency discharge, and microwave discharges. Among various thermal plasmas, arc plasma with high energy efficiency has been applied to welding, cutting, plasma spraying, plasma metallurgy, plasma densification such as spheroidization, nanomaterial fabrication, and waste treatment. In particular, DC power supplies are usually utilized to generate arc plasmas [5, 6], although converting AC to DC requires larger energy cost than AC power supplies [7, 8]. The commercially existing single-phase or three-phase AC power supplies have a characteristic of intermittent discharge due to the polarity transition, resulting in a momentary zero current. This characteristic limits the application of the arc plasma. A multiphase AC power supply was developed to overcome this limitation. A stable 12-phase AC arc was successfully generated, which possesses following advantages: high energy efficiency, large plasma volume, low gas velocity, and low cost [9, 10].

Fundamental phenomena in the multiphase AC arc has been revealed by experimental works with a high-speed camera technique [11-14]. Arc fluctuation was clarified by image analysis [11]. Characteristic arc swing motion due to rotational electric field of multiphase alternating current has been reported [12]. Moreover, controllability of high-temperature arc region by multiphase electrode configuration was discovered [13, 14].

Temperature field and its fluctuation in the multiphase arc was investigated on the basis of the high-speed camera system with band-pass filters [15-17], which transmit an emission at particular wavelength. Two synchronized images corresponding line emissions from atomic argon at different wavelengths were visualized. Temperature field was visualized through the relative intensity method. Effect of operating parameter of the multiphase AC arc such as driving frequency, ambient pressure, and arc current on the temperature fluctuation has been revealed. Temperature of the multiphase AC arc at near the electrode was higher than 10,000 K while that at the center region of the furnace was about 7,000 K, which is still sufficiently high to melt/evaporate refractory metals or ceramics.

The multiphase AC arc is considered to be utilized for the purpose of the energy saving. In-flight glass melting technology is one of the most important processing with the multiphase AC arc [18-24]. Granulated powders of glass raw materials such as silicon dioxide are injected into the high-temperature region of the multiphase AC arc. Vitrification process of the glass raw materials can be completed within the residence time about tenth to hundred milliseconds in the multiphase AC arc due to its sufficiently high temperature of the in-flight particles [25, 26].

Nanomaterial synthesis is also considered as suitable material processing by the multiphase AC arc [9]. While researches on the nanofabrication through the multiphase AC arc is still few, formation mechanism of the nanoparticles in other thermal plasmas has been studied numerically and experimentally, especially metals or intermetallic compounds nanoparticles [27-31]. Nanoparticle formation mechanisms of metal silicide [32-35] and metal boride [36-38] have also been successfully understood. Investigation on Si-M (Mo, Ti, Co, Fe, Cr, V, and Mn) system has been reported, while that on B-M (Al, Ti, Fe, Co, Cr, Ni, Mn, Y, Nb, Mo, Ta, W, and La) has also been reported.

Metal oxide nanoparticles, in contrast, remains to be understood because the oxidation process during rapid quenching in thermal plasmas is complex. In order to solve this issue, high-speed visualization of precursors in thermal plasma has been developed in recent. High-speed camera visualization with an imaging spectrometer was utilized to understand the fundamental phenomena in pulse-modulated induction thermal plasma [39-40]. Emissions from titanium atom, titanium monoxide were clearly visualized at the appropriate wavelengths. Two dimensional distributions of excitation temperature of titanium atom was successfully obtained. However, there are only few researches about metal oxide nanoparticle formation in the multiphase AC arc. Synchronized visualization of aluminum atom and aluminum monoxide molecule in the multiphase AC arc has been conducted [41], while the understanding of the formation mechanism of metal oxide nanoparticles are still unclear.

The objective of this study is to elucidate the formation mechanism of metal oxide nanoparticles in the multiphase AC arc. First, suitable metal oxide system was selected on the basis of the thermodynamic discussion as well as a spectroscopic diagnostics. Second, temperature measurement of the multiphase AC arc during nanoparticle synthesis was carried out. Then, the visualization of the precursor for metal oxide nanoparticles was conducted to understand the formation mechanism of the metal oxide nanoparticles in the multiphase AC arc.

2. Experimental methods

2.1 Experimental setup and procedure

Figure 1 present a conceptual illustration of the multiphase AC arc reactor, which consists of an arc chamber, multi-electrodes, AC power supplies at commercial 60Hz, and a powder feeder. Twelve electrode can be potentially installed from the side wall of the plasma reactor, while 6 electrodes are introduced in the present study. These 6 electrodes were symmetrically arranged by an angle of 60 degrees and were placed at an angle of 5 degrees from the horizontal plane. Each electrode with diameter of 6 mm was made of W (98wt%) and metal oxide (2wt%). Lanthanum oxide, La_2O_3, was doped in tungsten to reduce the effective work function for stable thermionic emission. Water at room temperature was used to cool the electrodes at 3 L/min of flow rate for each electrode. Air was utilized as plasma forming gas, while Ar gas with 99.99% in purity was injected around each electrode at 10 L/min of gas flow rate to prevent them from the oxidation. The multiphase AC arc was generated under the atmospheric pressure. Arc current was changed as operating parameter in the range from 80 A to 180 A for each electrode.

2.2 Raw material

Raw powders with micron-scale were injected into the multiphase AC arc by the powder feeder as shown in Fig. 1. Powders of Al, W, La_2O_3, and CeO_2 were selected as raw materials of each metal oxide nanoparticles. These raw materials were selected in terms of (a) the powder feeding stability and (b) the existence of metal oxide in vapor phase. In particular, the existence of stable metal monoxide in vapor phase is important to visualize the precursor of the nanoparticles in thermal plasma. The reason why raw materials include both pure metal and metal oxide is as follows. The amount of the oxygen from metal oxide as raw materials are much smaller than that of the oxygen derived from air as the plasma forming gas. Therefore, the effect of oxygen from metal oxide raw material on the metal oxide nanoparticle formation can be negligible. The raw material was fed into thermal plasma region by Ar carrier gas in 5 L/min of flow rate at a fixed feed rate of 2 g/min.

Above-mentioned raw powders were instantly evaporated just after these were injected into thermal plasma region. Then, monomer, metal vapor or metal oxide molecule, reached to super-saturated state during quenching process, resulting in the homogeneous nucleation. Heterogeneous co-condensation occurred after super-saturated monomer nucleated. Remained metal and/or metal oxide is co-condensed onto these nucleus, forming metal oxide

nanoparticles.

2.3 Measurement system

Figure 2 shows a measurement equipment which consisted of a high-speed camera (FASTCAM SA-5, Photron Ltd., Japan) and band-pass filter optics (MSI-2, Photron Ltd., Japan). Observation of the particular emission from thermal plasmas is strong method to understand fundamental phenomena in thermal plasmas, however, it is conventionally difficult because the strong radiations based on different emission mechanisms accompany with the objective emissions. In the present study, synchronized observation of particular species at two different wavelengths was achieved by utilization of appropriate band-pass filters. Emissions from metal, metal oxide, and argon were observed. Observation wavelengths including band-width of the selected filters will be explained in the results section 3.1. Frame rate and shutter speed for visualization were fixed at 1,000fps and 0.2 ms, respectively. The arc voltage and current waveforms were also measured at an sampling rate of 1MHz by an oscilloscope (Scope Corder DL 850, Yokogawa, Japan) synchronized with the high-speed visualization.

Excitation temperature of selected metal was also conducted by the same optical system mentioned above. The principal and the selected emissions for temperature measurements will be explained at section 3.2 on the basis of the obtained experimental results.

Spectroscopic measurements (iHR550, Horiba Jobin Yvon, Japan) were conducted and the transmission wavelengths of the filters were selected for visualization of the precursor in the multiphase AC arc as well as for the temperature measurements. Measurement positions at different distances from electrodes were shown in Fig. 1(b). Measurement area was about 1 mm^2.

3. Results and discussion

3.1 Selection of appropriate raw material

Suitable metal-oxygen system for the high-speed visualization was discussed according to following criteria. Thermodynamic stability of metal oxide molecule in vapor phase at temperature range from 3,000 to 6,000 K under atmospheric pressure is first criterion. Second is the emission intensity from molecular spectrum. In particular, that in visible wavelength range was checked because of the detectivity of the camera equipment. Figure 3 presents temperature dependence of the Gibbs free energy change of oxidation for considered metals. Obtained results showed that stable oxide in gas phase exist in the

systems of Al-O, La-O, and Ce-O, while metal oxide in W-O system is unstable at the considered temperature range.

Figure 4 shows the emission spectra with different metal oxide systems, (a) Al-O, (b) La-O, (c) Ce-O, and (d) W-O. Band emissions from AlO, LaO, and CeO were observed. In contrast, that from WO was not found. Correlation between the relative emission intensity form metal monoxide and the Gibbs free energy change at 5,000 K is shown in Fig. 5. Here, strongest emission intensity in visible range was chosen for each system to find an optimum system for high-speed visualization. Higher intensity of metal monoxide emissions accompanies with lower Gibbs free energy change. Therefore, La-O system was selected in this study. Here, synthesized nanoparticles in this system was La_2O_3 in the multiphase AC arc under air atmosphere. The precursor of La_2O_3 nanoparticles in thermal plasma is focused on the present study.

Figure 6 indicates the emission spectra of the multiphase AC arc observed at 30 mm from the electrode for different wavelength ranges. Strong emissions from La atom and La ion were found. The transmission wavelength for La atom was selected as 625.0 ± 1.0 nm to transmit the only emission from La atom at 624.993 nm with negligible emissions from others such as La ion. On the other hand, Fig. 6(b) presented strong emissions from LaO. Transmission wavelength for LaO molecule with band head of 740.35 nm was selected to be 740.0 ± 1.0 nm.

3.2 Visualization of temperature field

Temperature field of the multiphase AC arc is important to understand the dynamic behavior of metal vapor and its oxide during nanoparticle formation process. High-speed camera system was applied to visualize the temperature field because time resolution of conventional temperature measurement by spectrometer is insufficient to follow the fluctuation of the multiphase AC arc. However, the spectral resolution of the high-speed camera measurement depends on the spectral interval of band-pass filter such as 1.0 to 10.0 nm, which is much wider than the spectral resolution of conventional spectrometer such as 0.01 to 1.0 nm. Therefore, a combination of two spectral intervals which include several line emissions was selected to estimate the temperature field of the multiphase AC arc during La_2O_3 nanoparticle formation.

Intensity ratio method was applied to estimate the temperature. Two spectral intervals, 625.0 ± 1.0 nm and 625.0 ± 2.0 nm, were selected. The intensity ratio of two spectral intervals can be expressed as in Eq. (1):

$$(Relative\ Intensity) = \frac{\varepsilon_{625.0\pm2.0}}{\varepsilon_{625.0\pm1.0}} = \frac{\varepsilon_{624.99} + \varepsilon_{626.60} + \varepsilon_{626.23}}{\varepsilon_{624.99}}. \quad (1)$$

Three line emissions were included in the wavelength range between 624.0 and 626.0 nm. In order to correlate the temperature to relative intensity, theoretical emission coefficients of each line emission was estimated. Figure 7 shows the theoretical emission coefficients of La atom at 624.99 and 626.60 nm and that of La ion at 626.23 nm, which were calculated from Eq. (2):

$$\varepsilon_{ki} = \frac{A_{ki} g_k}{\lambda} \frac{\mathrm{hc} N(T)}{4\pi Z(T)} \exp\left(-\frac{E_k}{\mathrm{k}T}\right), \quad (2)$$

where $N(T)$ is the number density of considered species, which was calculated on the basis of the equilibrium composition under the following assumption. Partial pressure of La related species, La atom and La ion, was assumed to be uniform in discharge region at 0.5 kPa, which was calculated from the ratio of La feed rate to the flow rate of plasma forming gas in discharge region. This method takes into account to different species, both La atom and ion, partition function $Z(T)$ should be considered. It was calculated from Eq. (3) with energy level E_k at state k state based on the statistical weight g_k, which were referred from [42].

$$Z(T) = \sum_k g_k \exp\left(-\frac{E_k}{\mathrm{k}T}\right). \quad (3)$$

Estimated temperature distributions and corresponding high-speed snapshots at 625.0 ± 1.0 nm during a half AC period with different arc currents are summarized in Fig. 9. Temperature was higher than 6,000 K at 0 mm from the plasma torch, and then decreases with an increase of the distance from the torch. Moreover, higher arc current leads to higher temperature and larger high temperature region.

Time-averaged axial temperature distribution at different arc currents is presented in Fig. 10. Temperature decreases until 5,000 K at about 40 mm with 80 A of arc current, while that decreases at about 70 mm with 180 A of arc current. This is reasonable because of the larger Joule heating at higher arc current. Boltzmann plot method using the conventional spectrometer was also applied to validate this high-speed measurement. Four line emissions from La atom at 521.186, 527.642, 624.993, and 626.602 nm were taken into account to estimate the temperature profile in axial direction at 80 A of arc current. Results showed the similar trend between the intensity ratio method by the high-speed camera and Boltzmann plot method by the spectrometer, although the lower limitation of temperature measurement by high-speed camera was about 5,000 K due to the detection limitation. This also validated that the rough assumption about the partial pressure mentioned above was not far from the

real phenomena. These validated temperature profiles in different arc currents are important to understand the nanoparticle formation mechanism quantitatively because the emission intensity from the precursor strongly depends on both the its temperature and concentration. Still, more precise temperature information is essential and currently under investigation.

3.3 Visualization of precursor of metal oxide nanoparticles

Representative high-speed snapshots of La and LaO in the multiphase AC arc with different arc currents during a half AC period are shown in Fig. 11. In both arc current cases, strong emission from LaO was clearly visualized at a wide area in a measurement region where the distance from the plasma torch was 0 to 100 mm. In contrast, strong emission from La atom was found only at the upstream region. This different observation region was can be explained the starting position of the oxidation. Lanthanum oxidation started at lower temperature region.

Figure 12 shows the time-averaged intensity distributions from La tom and LaO molecule with different arc currents. An increase of arc current led to wider existence region of La atom. This can be explained by the expanded high temperature region in the case with higher arc current as indicated in Figs. 8 and 9. In contrast, the stronger intensity of LaO was also found in the region near the electrode in the case of 180 A. This is not the intensity from LaO, but from continuum emission of the high-intensity arc at the high electron number density near the electrode.

Relative intensity of La to LaO emissions was calculated from the high-speed snapshots to estimate relative number density of LaO molecule to La atom. Figure 13 shows the relative intensity distributions of LaO to La with different arc currents. The higher relative intensity was found at the downstream in both arc current cases. Results also suggested the relative intensity fluctuated on millisecond timescale. This fluctuation can be explained by two reasons. One is the fluctuation of 6-phase AC arc at 3.33 ms, which was reported in our previous work [17]. Another is the fluctuation of powder feeding. This fluctuation is still in under investigation.

Time-averaged distributions of the relative intensities of LaO to La at different arc currents were estimated and shown in Fig. 14. Axial distribution of relative intensity of LaO to La at 180 A was different from 80 A. This difference can be explained from the different axial temperature distributions in each case. Relative intensity of LaO to La at 80 A of arc current was almost unity at the 30 mm from the electrode where the temperature was about 5,500 K. On the other hand, Relative intensity of LaO to La at 180 A of arc current was almost unity

at the 70~80 mm from the electrode where the temperature was also about 5,500 K. This fact indicated that the relative intensity profile can be explained by the temperature profile, suggesting that the La oxidation in thermal plasma occurred with following thermodynamic equilibrium.

Temperature field of the multiphase AC arc and the oxidation process of La vapor were visualized through the high-speed camera system. Oxidation process from La to LaO in vapor phase was focused, while the final products in this process was La_2O_3 nanoparticles. Obtained experimental results revealed the formation mechanism of La_2O_3 nanoparticles in thermal plasma as summarized in Fig. 16. Oxidation from La to LaO occurred during quenching process around 5,200 K with following the equilibrium composition. Then, LaO nucleation triggers the condensation of LaO remained in vapor phase and their further oxidation into La_2O_3. These fundamental understanding will be important to control phase and size of the nanoparticles, although these still remained to be explored.

4. Conclusions

The dynamic behavior of precursor of the metal oxide nanoparticles, lanthanum and lanthanum monoxide, in the multiphase AC arc was successfully visualized by the high-speed camera with band-pass filters. The transmission wavelengths of 625.0 ± 1.0 nm and 740.0 ± 1.0 nm for La and LaO, respectively, were determined. Furthermore, the temperature field of the multiphase AC arc during raw powder injection was visualized based on the relative intensity method which includes the emissions from La atom and La ion. Obtained temperature profile and the intensity profile of La and LaO suggested the oxidation from La to LaO occurred at around 5,200 K with following the equilibrium composition. These understanding enables to expand the capability of thermal plasma for nanomaterial fabrication process at sufficiently high productivity.

Acknowledgment

This work was partially supported by JSPS KAKENHI Grant Number (C) JP19K03808.

References

1) T. Watanabe, Narengerile, and H. Nishioka, Plasma Chem. Plasma Process. **32**, 123 (2011).
2) M. Shigeta and A. B. Murphy, J. Phys. D: Appl. Phys. **44**, 170425 (2011).

3) J. Heberlein and A. B. Murphy, J. Phys. D: Appl. Phys. **41**, 053001 (2008).
4) O. Živný, M. Hlína, A. Serov, A. Halinouski, and A. Mašláni, Plasma Chem. Plasma Process. **40**, 309 (2020).
5) M. Tanaka and T. Watanabe, Jpn. J. Appl. Phys. **53**, 076201 (2013).
6) M. Tanaka, H. Soeda, T. Watanabe, and K. Otsuki, J. Fluid Sci. Technol., **13**, JFST0027 (2018).
7) J. E. Harry and R. Knight, IEEE Trans. Plasma Sci. **516** 6645 (2008).
8) J. E. Harry and R. Knight, J. Phys. D: Appl. Phys. **516** 6645 (2008).
9) T. Matsuura, K. Taniguchi, and T. Watanabe, Thin Solid Films, **515,** p. 4240 (2007).
10) T. Watanabe, K. Yatsuda, T. Yano, and T. Matsuura, Pure Appl. Chem. **82** 1337 (2010).
11) M. Tanaka, Y. Tsuruoka, Y. Liu, T. Matsuura, and T. Watanabe, Current Appl. Phys. **11** S35 (2011).
12) M. Tanaka, Y. Tsuruoka, Y. Liu, and T. Watanabe, IEEE Trans. Plasma Sci. **39** 2904 (2011).
13) Y. Liu, M. Tanaka, S. Choi, and T. Watanabe, J. Appl. Glass Sci. **10** 443 (2014).
14) Y. Liu, M. Tanaka, T. Ikeba, S. Choi, and T. Watanabe, J. Chem. Eng. J. **46** 672 (2013).
15) M. Tanaka, T. Imatsuji, T. Hashizume, T. Watanabe, H. Nagai, T. Koiwasaki, and T. Okuma, J. Fluid Sci. Technol. **12** (3) JFST0024 (2017).
16) T. Okuma, T. Imatsuji, M. Tanaka, T. Hashizume, T. Watanabe, H. Nagai, and T. Koiwasaki, J. Fluid Sci. Technol. **13** (4) JFST0024 (2018).
17) T. Okuma, H. Maruyama, T. Hashizume, M. Tanaka, T. Watanabe, H. Nagai, and T. Koiwasaki, IEEE Trans. Plasma Sci., **47** (19), 32 (2019).
18) Y. C. Yao, T. Watanabe, T. Yano, T. Iseda, O. Sakamoto, M. Iwamoto, and S. Inoue, Sci. Technol. Adv. Mat. **9** 8 (2008).
19) Y. Yao, K. Yatsuda, T. Watanabe, F. Funabiki, and T. Yano, Chem. Eng. J. **144** 317 (2008).
20) Y. Yao, M. M. Hossain, T. Watanabe, T. Matsuura, F. Funabiki, and T. Yano, Chem. Eng. J. **139** 390 (2008).
21) F. Funabiki, Y, Yano, Y. Yao, and T. Watanabe, J. American Ceram. Soc. **91** 3908 (2008).
22) Y. Yao, M. M. Hossain, T. Watanabe, T. Tsujimura, F. Funabiki, and T. Yano, Thin Solid Films **516**, 6622 (2008).
23) Y. Liu, Y. Tsuruoka, M. Tanaka, T. Ichihashi, T. Yano, and T. Watanabe, Thin Solid Films **519** 7005 (2011).
24) M. Tanaka, Y. Liu, Y. Tsuruoka, and T. Watanabe, Thin Solid Films **523**, 67 (2012).
25) Y. Liu, M. Tanaka, S. Choi, and T. Watanabe, J. Therm. Spray Technol. **21** 863 (2012).

26) Y. Liu, M. Tanaka, T. Ikeba, S. Choi, and T. Watanabe, J. Phys. Conf. Seri. **406** 012022 (2012).
27) S. Ohno and M. Uda, J. Japan Inst. Metals, **48**, 640 (1984).
28) S. Ohno and M. Uda, J. Japan Inst. Metals, **53**, 946 (1989).
29) M. Tanaka and T. Watanabe, Thin Solid Films, **516**, 6645 (2008).
30) M. Shigeta and T. Watanabe, J. Appl. Phys., **108**, 043306 (2010).
31) Y. Ishisaka, N. Kodama, K. Kita, Y. Tanaka, Y. Uesuhi, T. Ishijima, S. Sueyasu, S. Watanabe, K. Nakamura, Appl. Phys. Express, **10**, 096201 (2017).
32) T. Watanabe, H. Itoh, and Y. Ishii, Thin Solid Films, **390**, 44 (2001).
33) T. Watanabe and H. Okumiya, Sci. Technol. Adv. Mater., **5**, 639 (2004).
34) M. Shigeta and T. Watanabe, J. Mater. Res., **20**, 2801 (2005).
35) M. Shigeta and T. Watanabe, Powder Technol., **288**, 191 (2016).
36) T. Watanabe, T. Ibe, Y. Abe, Y. Ishii, and K. Adachi, Trans. Mater. Res. Soc. Japan, **29**, 3407 (2004).
37) Y. Cheng, S. Choi, and T. Watanabe, Powder Technol., **246**, 210 (2013).
38) Y. Cheng, Y. Shigeta, S. Choi, and T. Watanabe, Chem. Eng. J., **183**, 483 (2012).
39) N. Kodama, Y. Tanaka, K. Kita, Y. Uesugi, T. Ishijima, S. Sueyasu, K. Nakamura, J. Phys. D: Appl. Phys., **49** (30), 305501 (2016).
40) N. Kodama, Y. Tanaka, K. Kita, Y. Ishisaka, Y. Uesugi, T. Ishijima, S. Sueyasu, K. Nakamura, Plasma Sources Sci. Technol., **26** (7), 075008 (2017).
41) M. Tanaka, Y. Saito, Y. Nawata, and T. Watanabe, J. Fluid Sci. Technol., **14** (3), JFST0024 (2019).
42) Kramida A, Ralchenko Y, Reader J and NIST ASD Team 2016, NIST Atomic Spectra Database (Version 5.4) (Gaithersburg, MD: National Institute of Standards and Technology)

Figure Captions

Fig. 1. (Color online) (a) Schematic illustration of experimental setup and (b) observation region.

Fig. 2. (Color online) Schematic illustration of high-speed visualization system.

Fig. 3. (Color online) Relationship between Gibbs free energy change and temperature for considered oxidation to monoxide. M+O=MO, M=Al, La, Ce, and W.

Fig. 4. (Color online) Emission spectra of the multiphase AC arc for different systems; (a) Al-O, (b) La-O, (c) Ce-O, and (d) W-O. Measurement position was 30 mm from the plasma torches.

Fig. 5. Relationship between Gibbs free energy change at 5,000 K and emission intensity from metal oxide. Measurement position was 30 mm from the plasma torches.

Fig. 6. (Color online) Emission spectra of multiphase AC arc during La_2O_3 powder injection. Measurement spot is located at 30 mm from the plasma torches.

Fig. 7. Theoretical emission coefficients of (a) La atom and (b) La ion.

Fig. 8. Theoretical relative intensity of the emissions at 625.0 ± 2.0 nm to that at 625.0 ± 1.0 nm.

Fig. 9. (Color online) High-speed camera images and their corresponding temperature distributions of the multiphase AC arc during La_2O_3 powder injection at different arc currents of (a) 80 A and (b) 180 A.

Fig. 10. (Color online) Axial temperature distributions of the multiphase AC arc during La_2O_3 powder injection.

Fig. 11. High-speed images of the multiphase AC arc through the band-pass filters with transmission wavelength of 625.0±1.0 nm for La vapor and 740.0±1.0 nm for LaO at different arc currents of (a) 80 A and (b) 180 A.

Fig. 12. (Color online) Time-averaged intensity from atomic La and LaO molecule at different arc currents; (a) 80 A and (b) 180 A.

Fig. 13. (Color online) Two-dimensional distributions of relative intensities of LaO to La.

Fig. 14. Axial distributions of time-averaged relative intensity of LaO to La at downstream from the electrode with different arc currents.

Fig. 15. (Color online) Formation mechanism of La_2O_3 nanoparticle in thermal plasma.

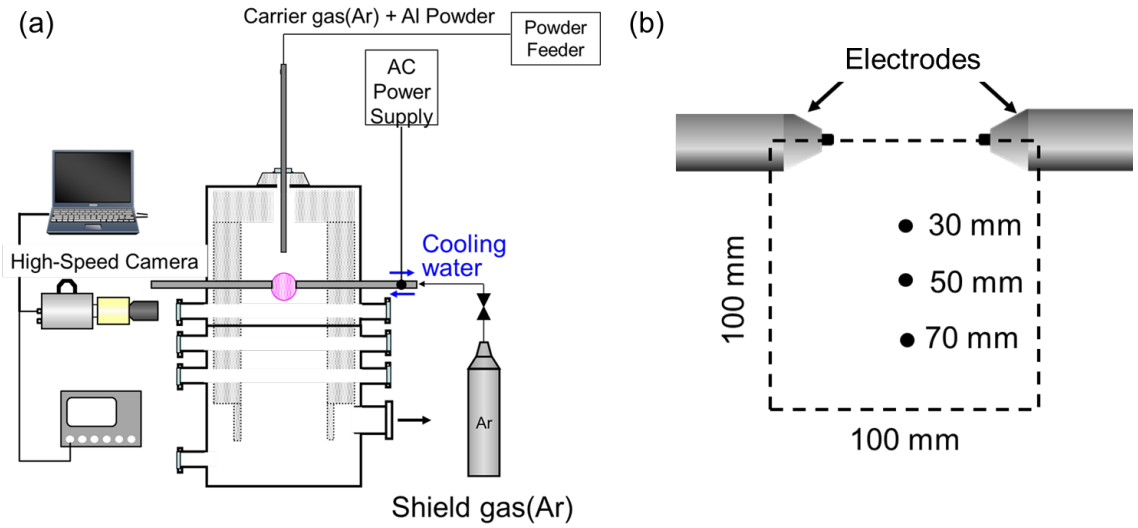

Fig.1. (Color online)

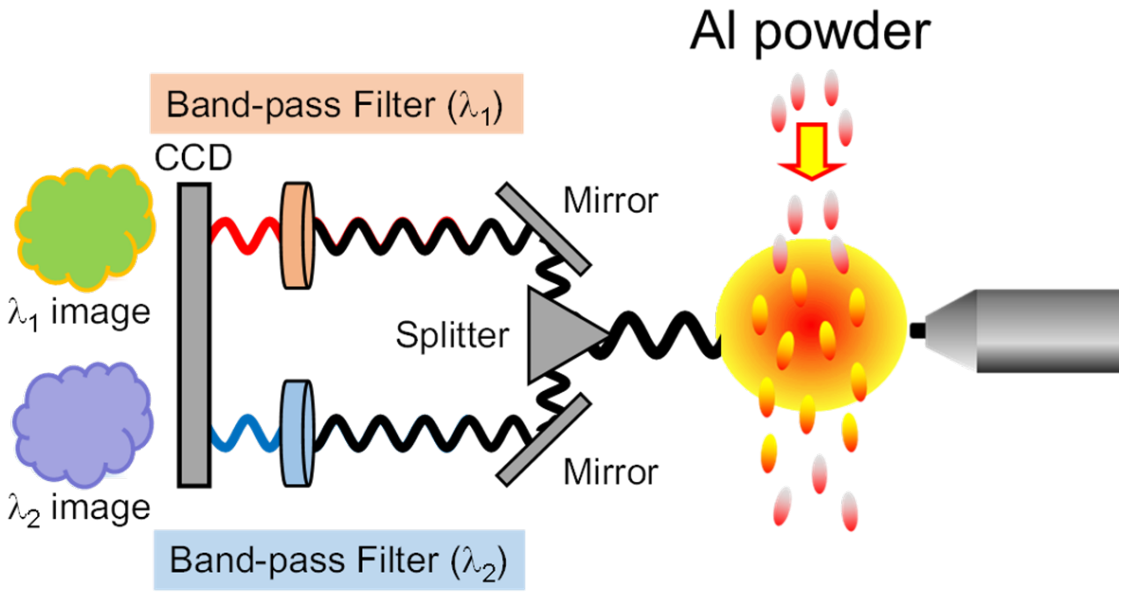

Fig. 2. (Color Online)

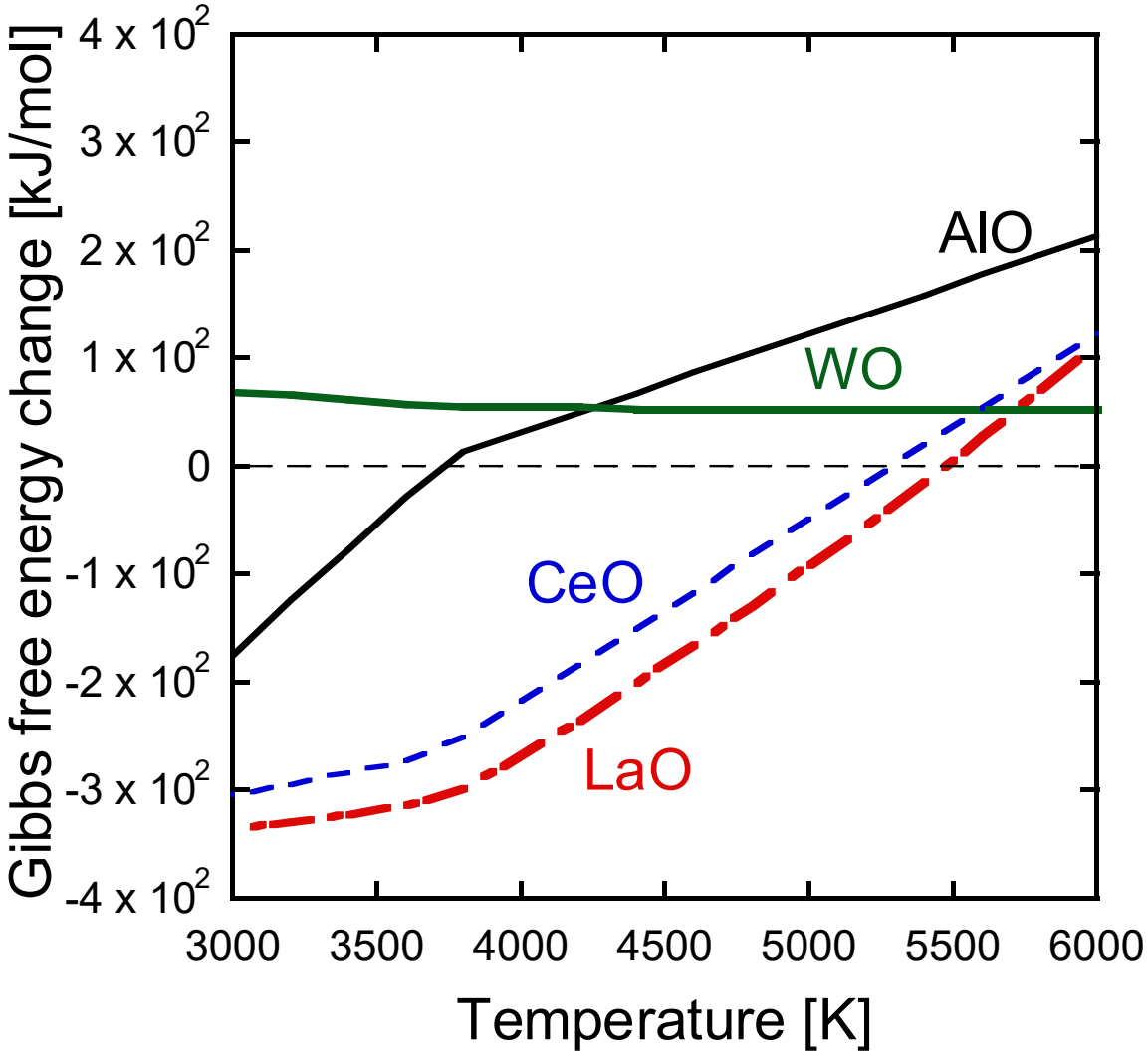

Fig. 3. (Color online)

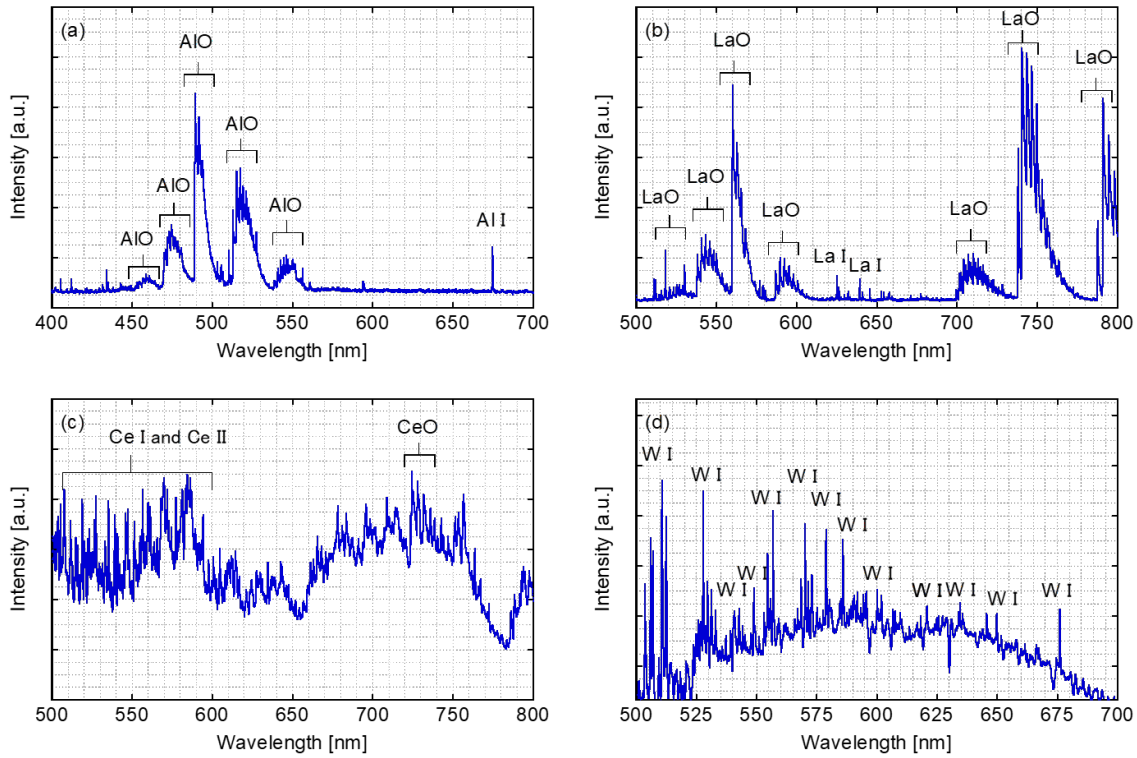

Fig. 4. (Color online)

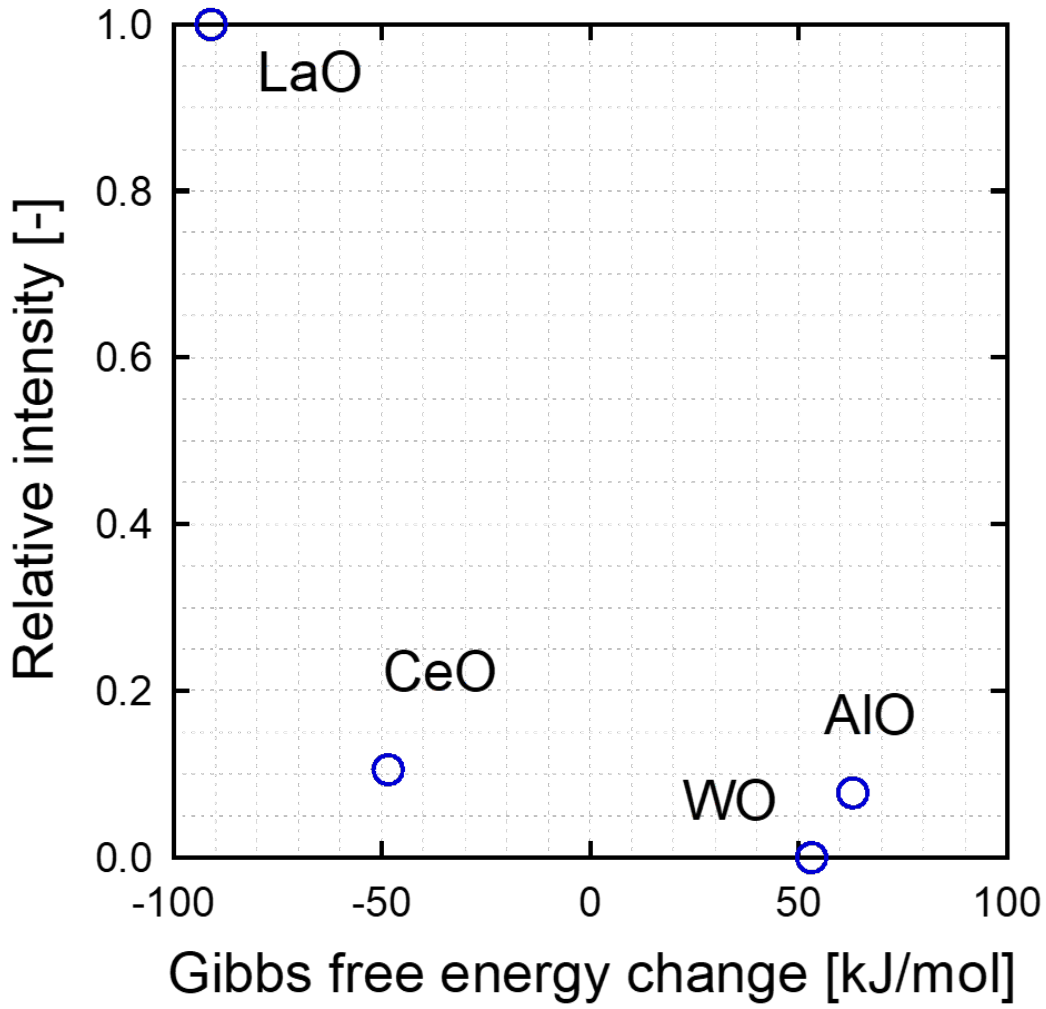
1.0
0.8
0.6
0.4
0.2
0.0
Relative intensity [-]
LaO
CeO
AlO
WO
-100
-50
0
50
100
Gibbs free energy change [kJ/mol]

Fig. 5.

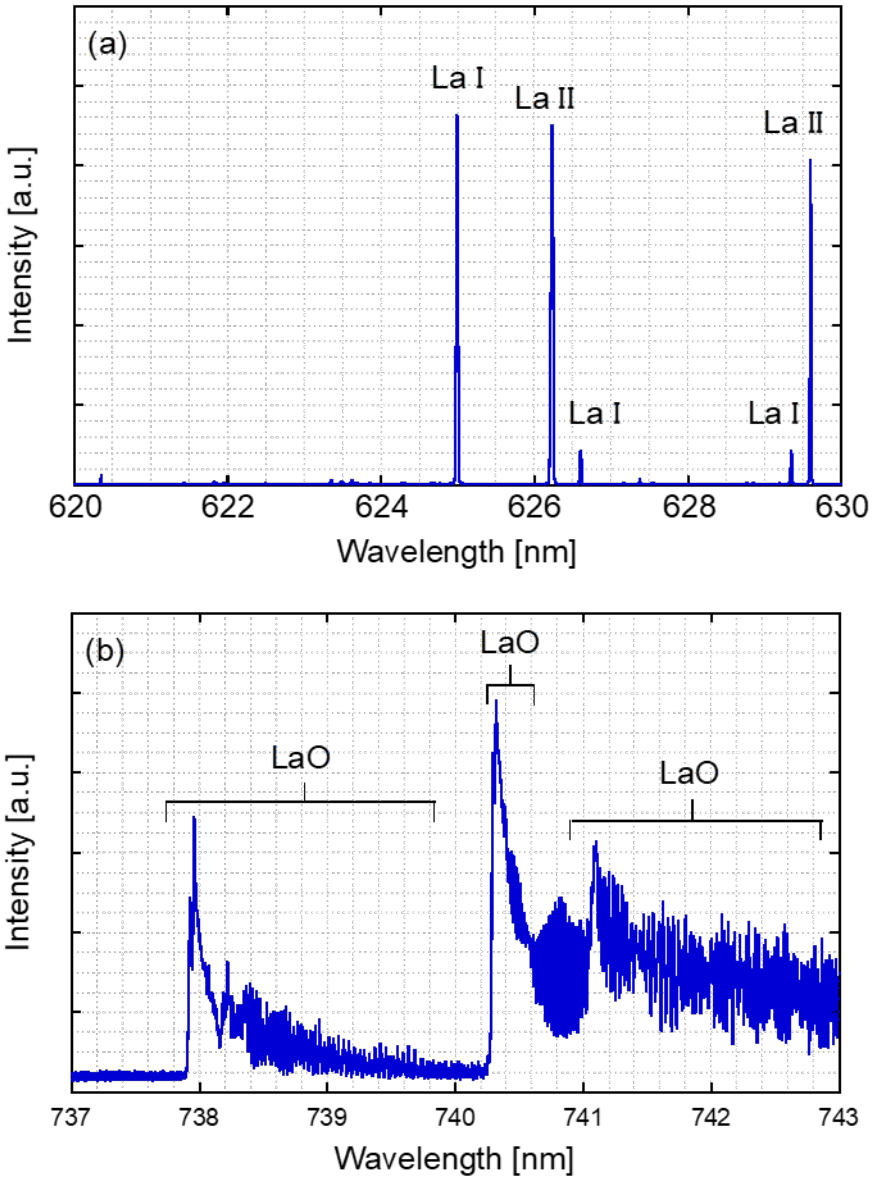

Fig. 6. (Color online)

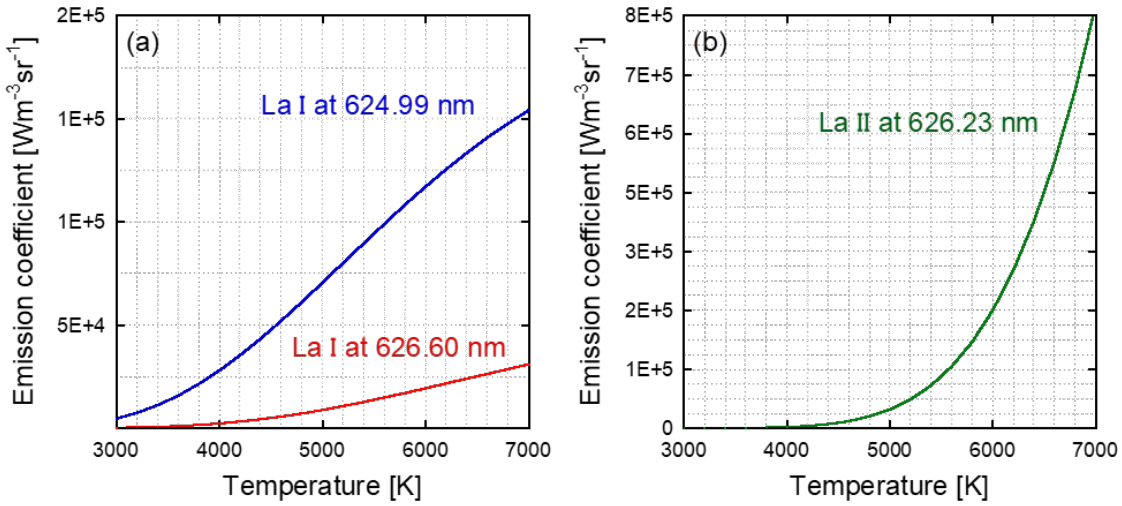
(a)
La I at 624.99 nm
La I at 626.60 nm
Emission coefficient [Wm-3sr-1]
Temperature [K]
2E+5
1E+5
1E+5
5E+4
3000
4000
5000
6000
7000
(b)
La II at 626.23 nm
Emission coefficient [Wm-3sr-1]
Temperature [K]
8E+5
7E+5
6E+5
5E+5
3E+5
2E+5
1E+5
0
3000
4000
5000
6000
7000

Fig. 7.

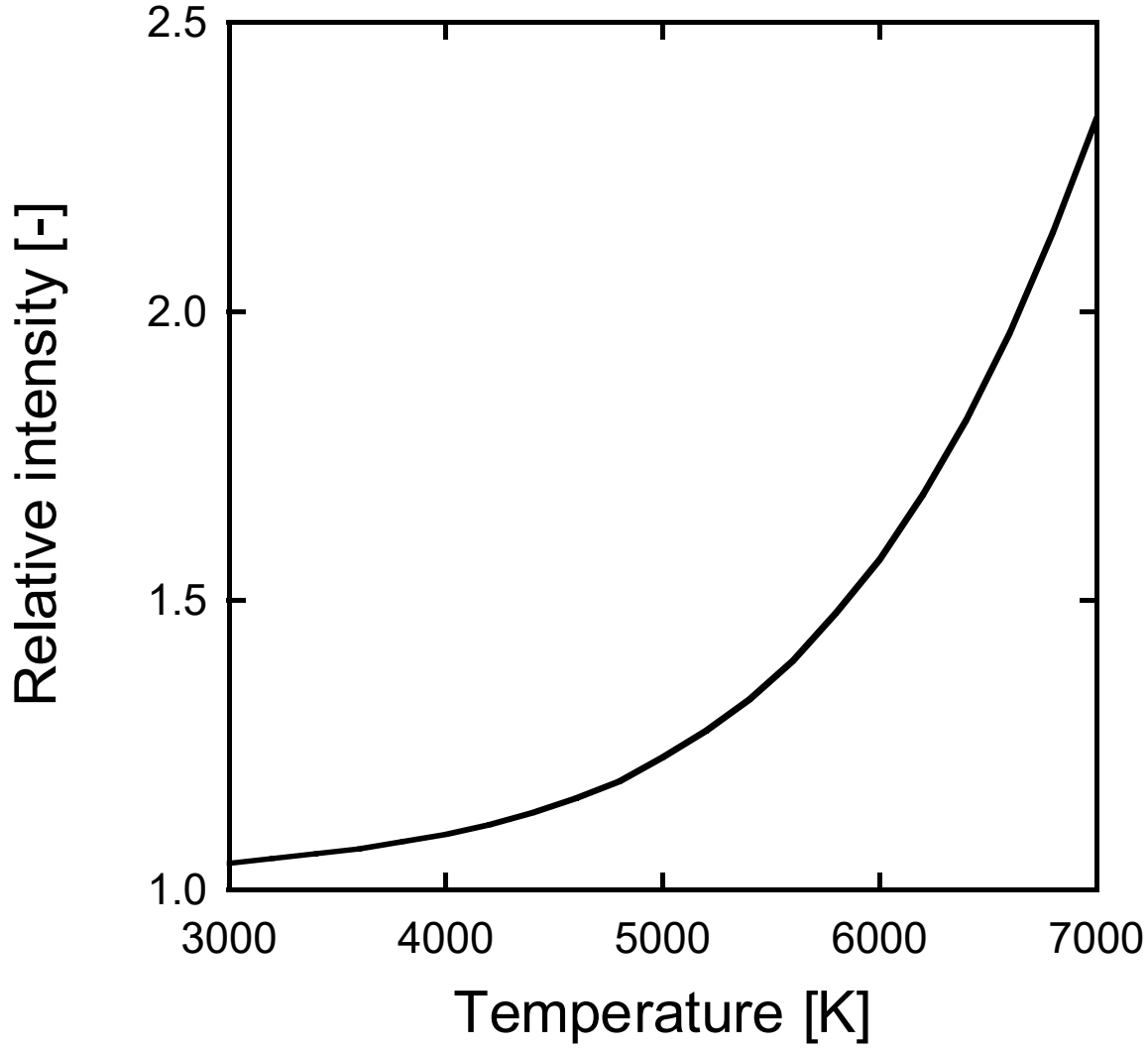
2.5
2.0
1.5
1.0
Relative intensity [-]
3000
4000
5000
6000
7000
Temperature [K]

Fig. 8.

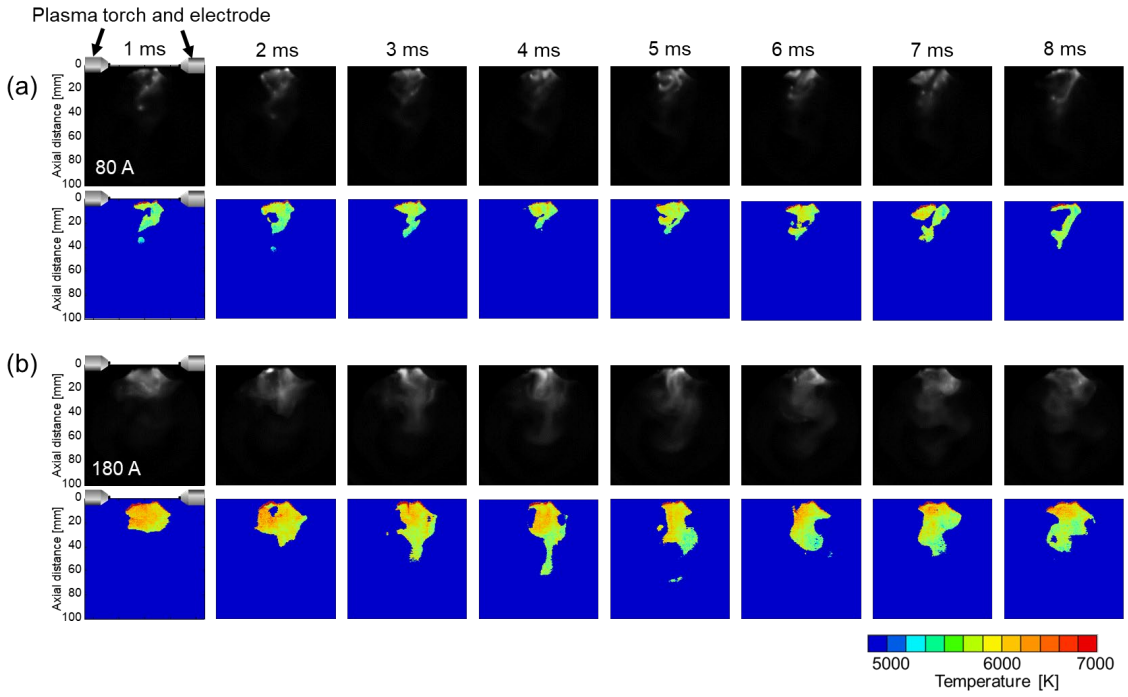

Fig. 9. (Color online)

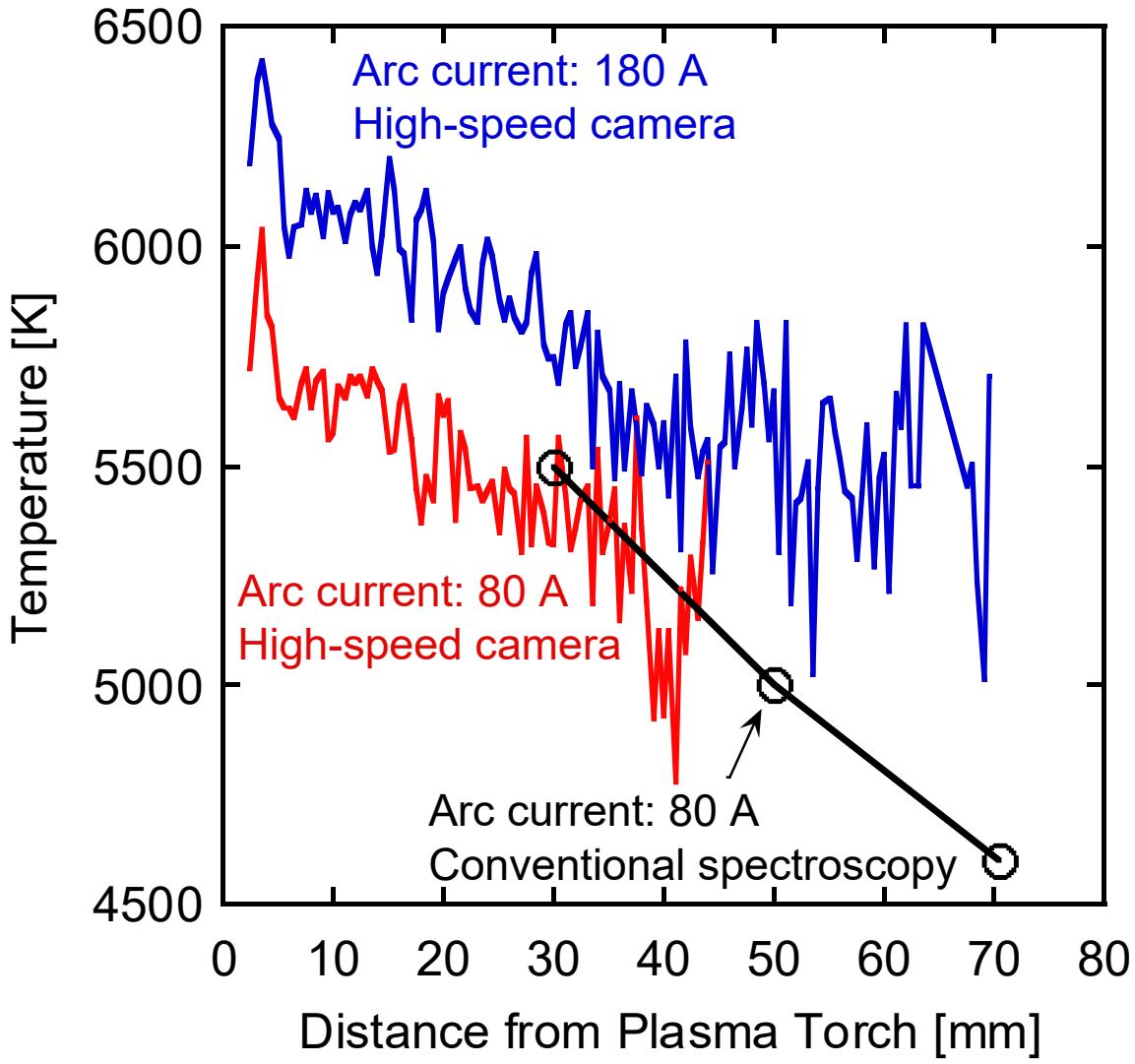

Fig. 10. (Color online)

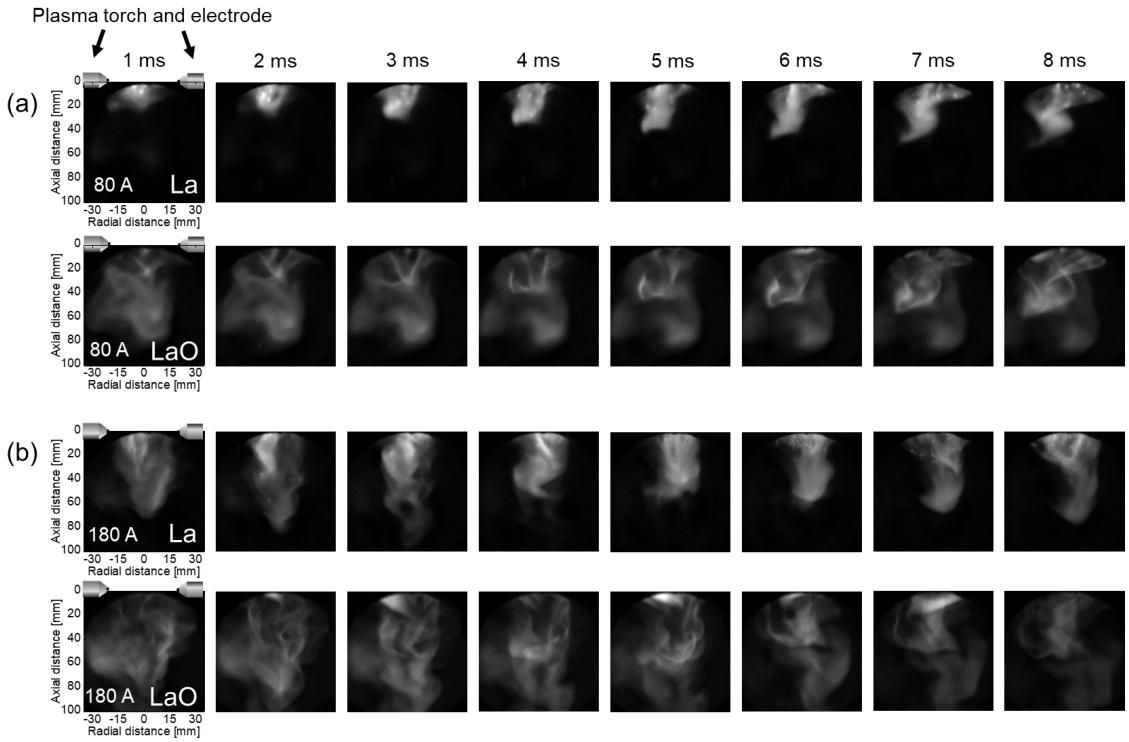
Plasma torch and electrode
1 ms
2 ms
3 ms
4 ms
5 ms
6 ms
7 ms
8 ms
(a)
80 A La
80 A LaO
(b)
180 A La
180 A LaO
Axial distance [mm]
Radial distance [mm]
0
20
40
60
80
100
-30 -15 0 15 30

Fig. 11.

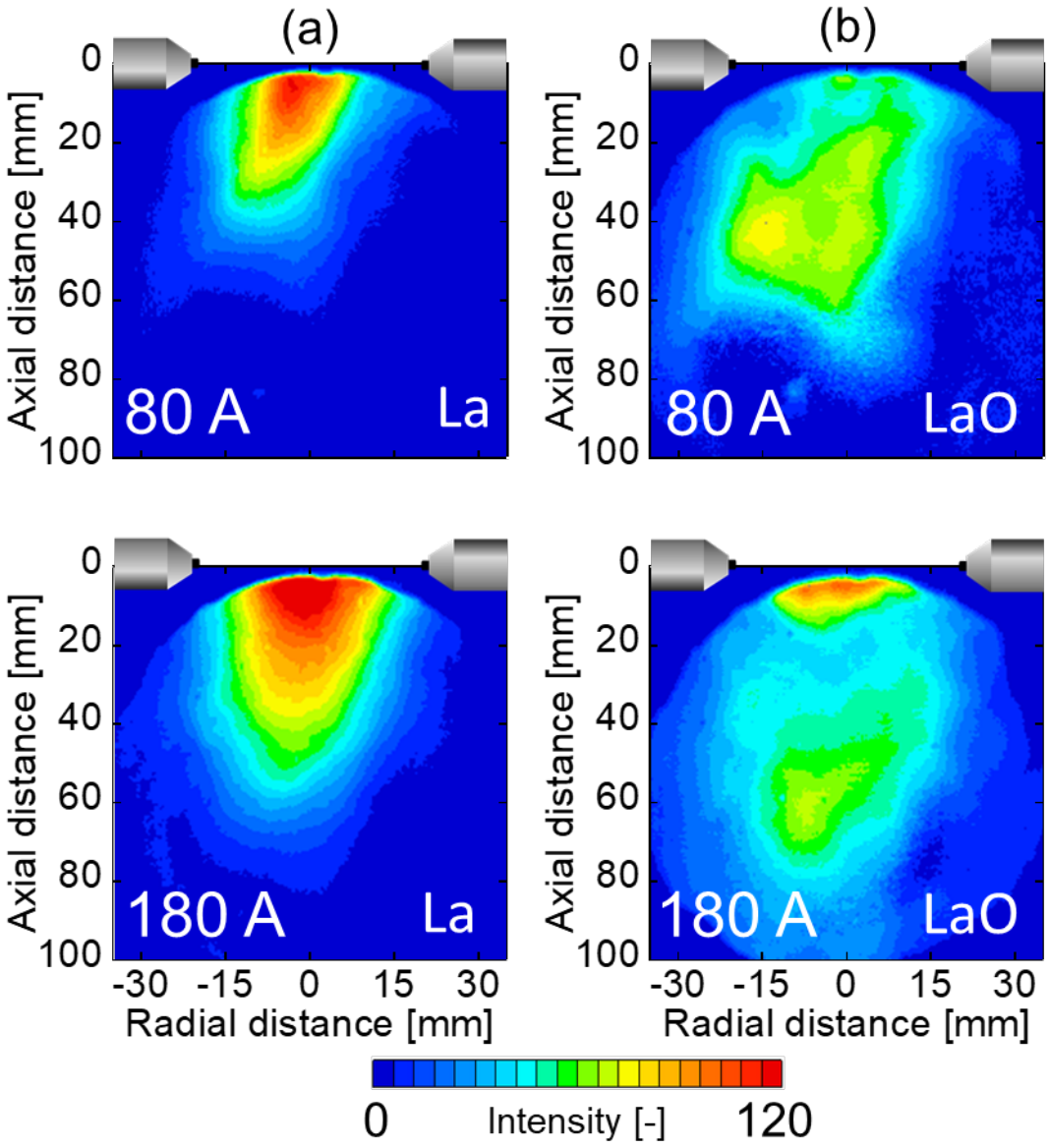

Fig. 12. (Color online)

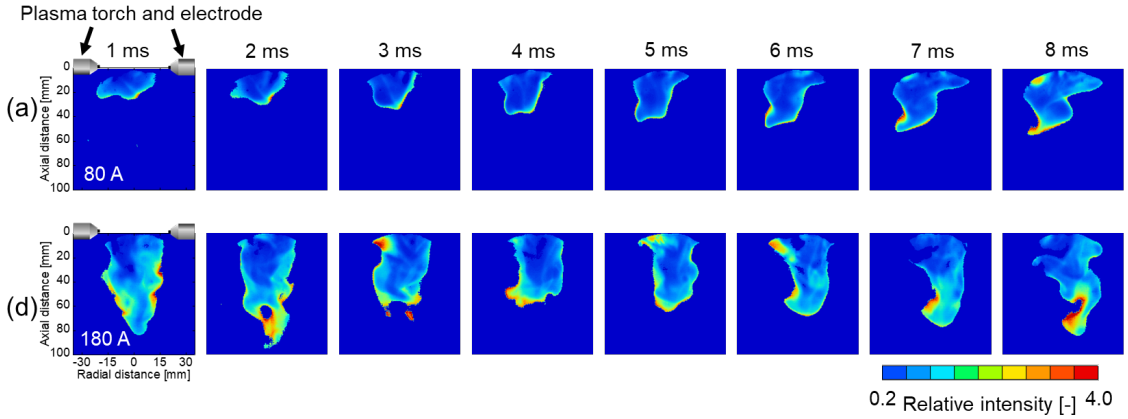

Fig. 13. (Color online)

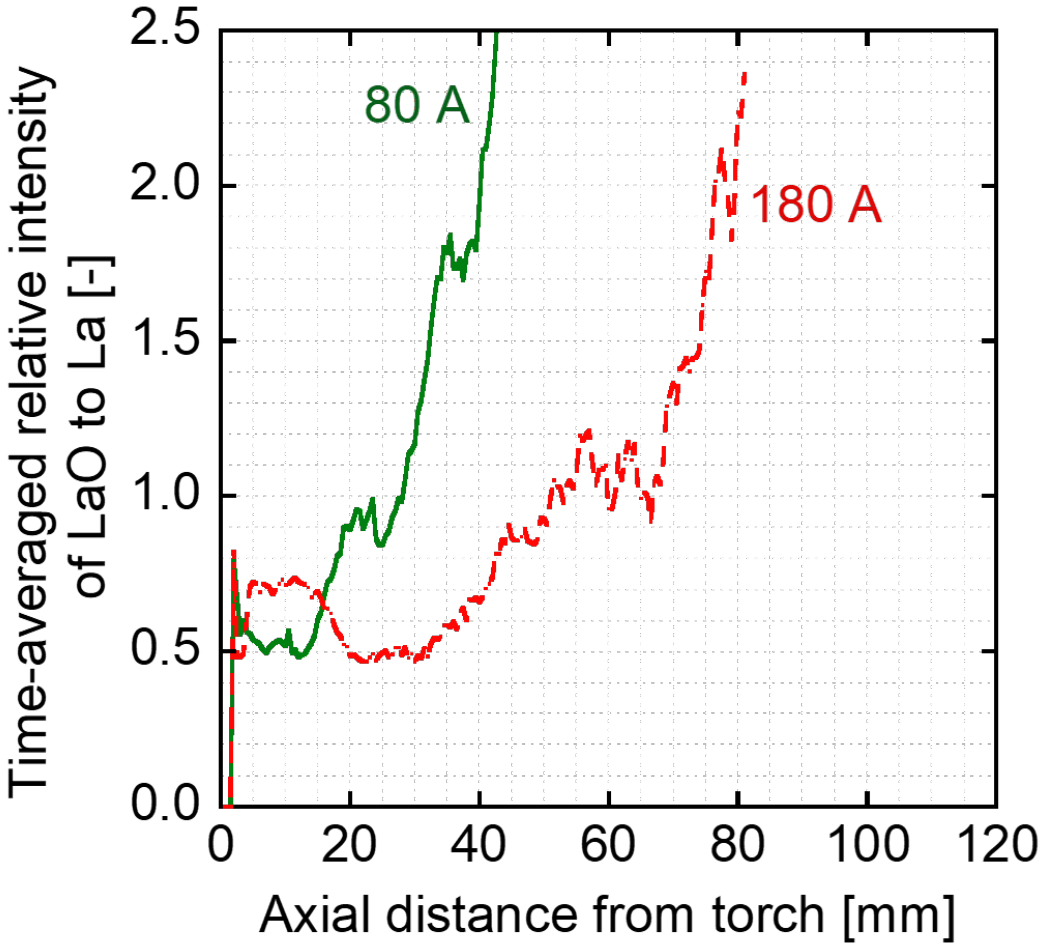
Time-averaged relative intensity of LaO to La [-]
2.5
2.0
1.5
1.0
0.5
0.0
0
20
40
60
80
100
120
Axial distance from torch [mm]
80 A
180 A

Fig. 14.

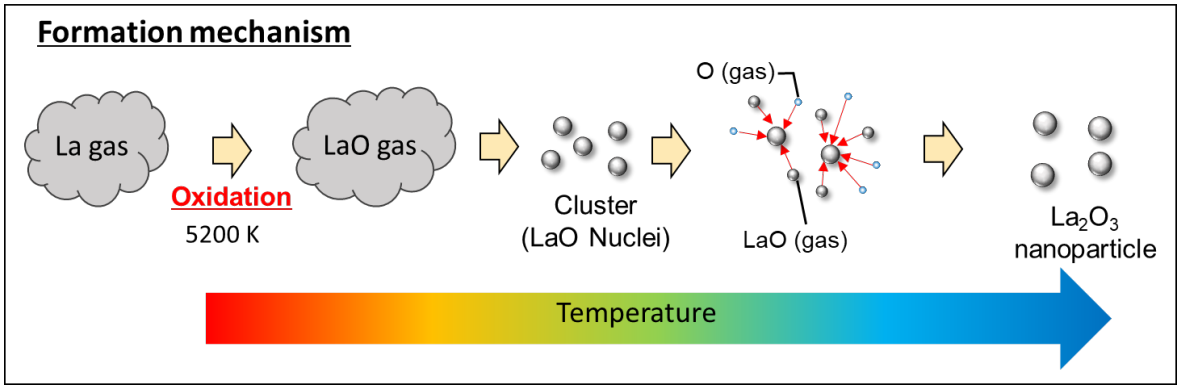

Fig. 15. (Color online)